Cryogenic-specific Reddish Coloration by Cryoplasma: New Explanation for Color Diversity of Outer Solar System Objects

Noritaka Sakakibara , Phua Yu Yu, Tsuyohito Ito , and Kazuo Terashima

Department of Advanced Materials Science, Graduate School of Frontier Sciences, The University of Tokyo, 5-1-5 Kashiwanoha, Kashiwa, Chiba 277-8561, Japan
n.sakakibara@plasma.k.u-tokyo.ac.jp, kazuo@plasma.k.u-tokyo.ac.jp

Abstract

Reddish coloration and color diversity among icy bodies in the outer solar system are significant clues for understanding the status and history of the solar system. However, the origin of color distribution remains debatable. Here, we demonstrate reddish coloration that is stable only at cryogenic temperatures in a laboratory experiment. The reddish coloration was produced on methanol- and water-containing ice irradiated with nitrogen-containing cryoplasma at 85 K. The reddish color visually faded and disappeared at 120–150 K as the ice was heated, unlike well-known refractory organic tholins that are stable even when heated to room temperature. This temperature dependence of reddish coloration under cryogenic conditions could provide a new possible explanation for the absence of ultra-red coloration closer to the Sun in the outer solar system. Our result implies that a reddish material specific to cryogenic environments is useful for the investigation of color diversity and the formation mechanism of the outer solar system.

Unified Astronomy Thesaurus concepts: Outer planets (1191); Trans-Neptunian objects (1705); Surface ices (2117)

1. Introduction

Reddish coloration and its diversity are significant characteristics widely observed in the outer solar system objects at larger heliocentric distances (Jewitt 2002b; Sheppard 2010; Stern et al. 2015, 2019; Weaver et al. 2016). Ultra-red objects occur only relatively far from the Sun such as some Centaurs and trans-Neptunian objects (TNOs), whereas Jupiter-family comets (JFCs) such as cometary nuclei and dead comets closer to the Sun lack the reddish coloration (Luu & Jewitt 1996; Sheppard 2010). Because there is color diversity among the objects despite both Centaurs and JFCs supposedly originating in TNOs (Duncan & Levison 1997; Lowry et al. 2008), ultra-red color materials have been explained to be sublimated or destroyed as the objects approach from the trans-Neptunian region to the inner solar system (Sheppard 2010). Accordingly, the reddish coloration and its distribution are significant for understanding the formation process of the solar system. Furthermore, it provides astrobiological insights into the origin of life (Khare et al. 1986; Cruikshank et al. 2019). The reddish color has been studied extensively in laboratory experiments and is attributed to complex refractory organic mixtures such as tholins, produced by energetic radiation on organic volatiles and their ice surfaces (Imanaka et al. 2004; Cruikshank et al. 2005; Materese et al. 2014, 2015). However, the tholin-type materials that have been studied are not volatile even when heated to room temperature. Due to this, explanation of the reddish color distribution is not straightforward. Although some alternative explanations for the reddish color distribution have been suggested (Jewitt 2002a; Grundy 2009; Brown et al. 2011), the color distribution is not fully elucidated and remains debatable (Dalle Ore et al. 2011).

In this study, we demonstrate the reddish coloration specific to cryogenic temperature in a laboratory experiment that is distinct from the well-known reddish coloration of the previously reported tholins. For the coloration, cryoplasma was radiated at 85 K on methanol (CH_3OH) and water (H_2O) containing ice by feeding helium (He) with 3% nitrogen (N_2). Cryoplasma is nonequilibrium plasma whose gas temperature can be controlled at wide range of cryogenic temperatures below room temperature (Stauss et al. 2018), enabling coexistence of plasma with ice without melting (Sakakibara & Terashima 2017; Sakakibara et al. 2019). This study roughly simulated energetic processes in the outer solar system via UV radiation and charged and/or excited species formed by cosmic rays and solar winds (Thompson et al. 1991; Imanaka et al. 2004). Although ultra-red coloration of TNOs has been experimentally reproduced by ion irradiation of methanol (Brunetto et al. 2006), in our study, reddish coloration that is stable only at cryogenic temperatures was obtained, as described below, which is definitively different from the previous study.

2. Experiment

2.1. Cryoplasma Irradiation of CH_3OH/H_2O Ice

In a custom-made cryogenic chamber equipped with a 4 K Gifford McMahon refrigerator (CKW-21, Sumitomo Heavy Industries), CH_3OH/H_2O ice grown on the top and bottom sides of the electrodes (Figure 1(a)) were irradiated with cryoplasma for 12 hr. The setup is similar to our previous study (Sakakibara & Terashima 2017). The top and bottom side of electrodes were composed of 150 μm thick indium tin oxide (ITO; 10 mm in diameter) coated glass and stainless steel (16 mm in diameter), respectively, with a gap distance of 500 μm. The CH_3OH/H_2O ice was used as a dielectric barrier to generate the cryoplasma in a dielectric barrier discharge configuration. To prepare CH_3OH/H_2O ice, a mixture of 200 μl of water (electrical conductivity <5 μS cm^{-1}, Wako pure chemical industries) and 200 μl of methanol (infinity grade, Wako pure chemical industries) was poured onto the ground electrode. The mixture was cooled at around 0.6 K minute^{-1} from room temperature to 80 K by lowering the ambient temperature in the chamber. Although the initial mixture had the same volume of CH_3OH and H_2O, the ice on the top electrode might be enriched in the more volatile CH_3OH than H_2O. Three percent N_2 gas (G1 grade) diluted with He gas (G1 grade) was pumped into the chamber at a 30 standard cubic centimeters per minute (sccm) flow rate as the

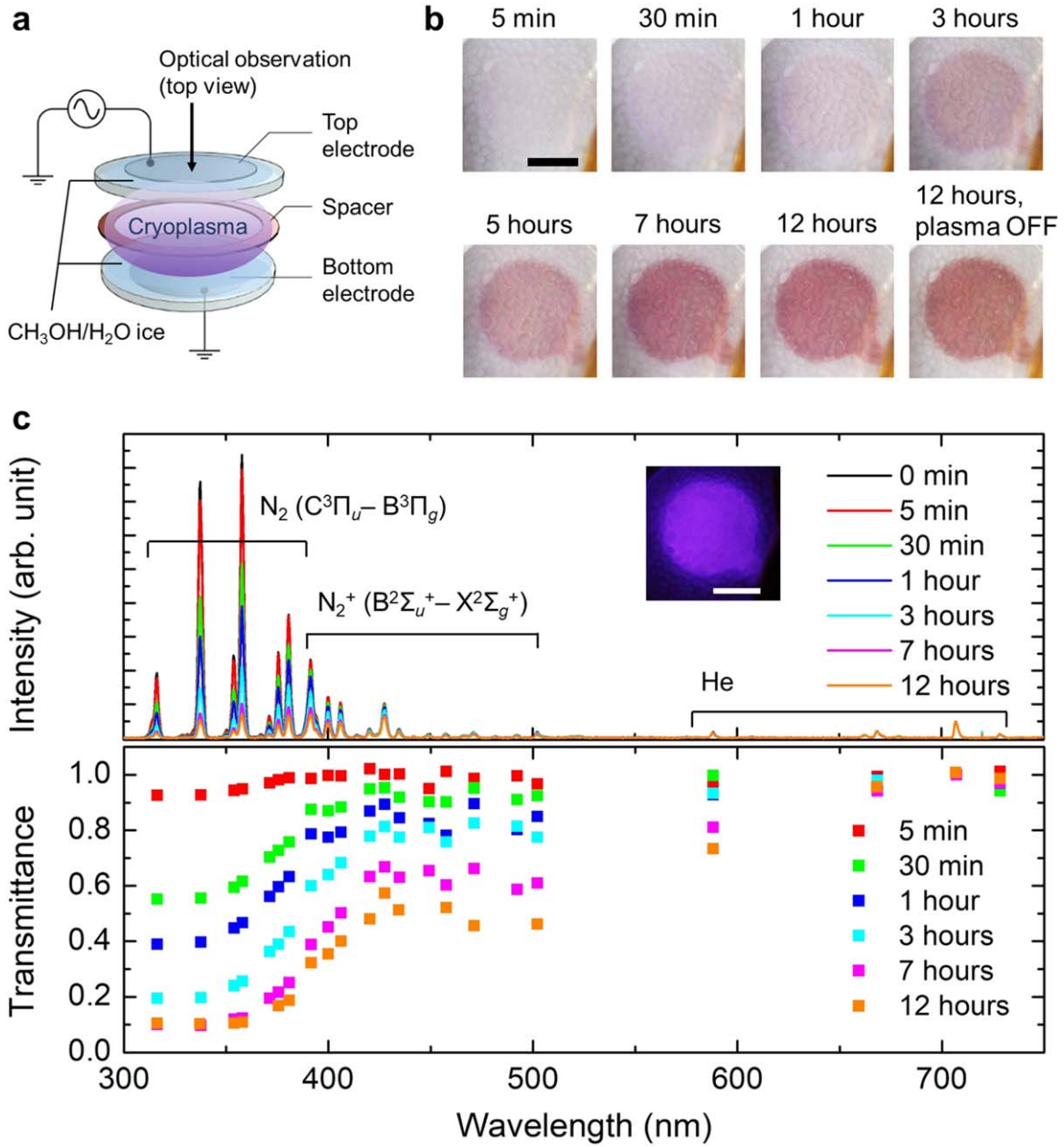**Figure 1.** Reddish coloration of the CH$_3$OH/H$_2$O ice during plasma irradiation. (a) Schematic illustration of the electrodes of the cryoplasma. (b) Photographs showing the changes in the reddish coloration of the ice during plasma irradiation. The reddish color was not the color of the plasma itself, as shown in the photograph taken after the plasma was turned off. The color was not degraded even after three days. The scale bar is 5 mm. (c) Optical emission spectra of the plasma (top panel) and transmittance of the ice (bottom panel) at different plasma irradiation durations. The transmittance at a given wavelength was calculated using the rate of decrease of the plasma emission intensity. The inserted photograph shows the top view of the cryoplasma. The scale bar is 5 mm.

carrier gas at 2×10^3 Pa. To generate the cryoplasma, 1.75 kV$_{pp}$ sinusoidal AC voltage was applied at 10 kHz to the top electrode with a function generator (WF1974, NF) and a high voltage amplifier (HVA4321, NF). The bottom electrode served as a ground electrode. He gas was utilized to stabilize the discharge and to offer better heat dissipation. The gas temperature of plasma was monitored by a silicon diode temperature sensor (DT470CU131.4L, Lakeshore) at 30 mm from the center of the cryoplasma, and it was maintained with proportional integral derivative (PID) control at 85 K with an accuracy of a few Kelvin (Sakakibara & Terashima 2017). The cryoplasma consumed 18.5 mW, indicating that the total energy transferred to the ice was 1.2×10^{-2} J cm^{-2} s^{-1}. For the 12 hr of plasma irradiation,

this dose corresponds to between 10^4 and 10^5 yr of energetic radiation such as solar wind in the assumption of 1 keV energies with between 10^9 and 10^{10} particles m^{-2} s^{-1} (Bagenal et al. 2016). The temperature, chemicals, and energetic radiation process chosen here are within the plausible range of current conditions of the outer solar system (Lewis 1973; Gilmore 2002; Bennett et al. 2013; Dalle Ore et al. 2015).

2.2. TPD Analysis of the Plasma-irradiated Ice

After the plasma irradiation of CH$_3$OH/H$_2$O ice, temperature programmed desorption (TPD) experiments were carried out with a quadrupole mass spectrometer with electron impact ionization (Prisma Plus QMG 220M1, Pfeiffer Vacuum). The
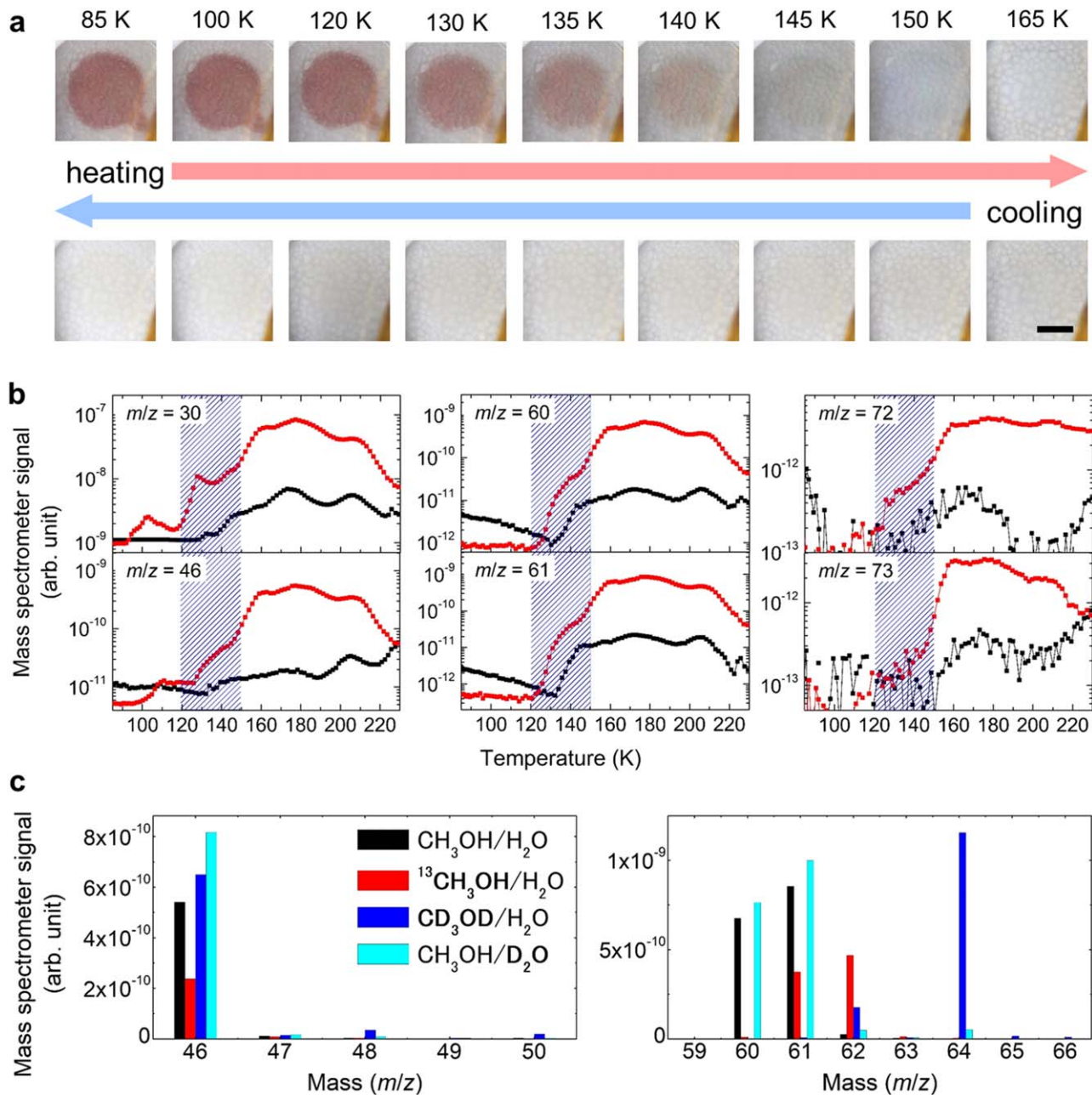
Figure 2. Heating of the post-plasma-irradiated CH$_3$OH/H$_2$O ice. (a) Photographs showing the disappearance of the reddish color during the heating. The scale bar is 5 mm. (b) TPD spectra indicating desorption of fragments from the post-plasma-irradiated ice. The red and black lines represent plasma irradiation with and without N$_2$ gas input, respectively. The blue shaded regions indicate the temperature range where the reddish color was seen to be disappearing. (c) Mass spectra of the isotope-labeled analysis of the post-plasma-irradiated ice. Mass spectra at 180 K are shown here. The black, red, blue, and cyan indicators represent the post-plasma-irradiated ice of CH$_3$OH/H$_2$O, ^{13}CH$_3$OH/H$_2$O, CD$_3$OD/H$_2$O, and CH$_3$OH/D$_2$O, respectively.

temperature in the chamber was increased at a linear heating rate of 1 K minute^{-1} from 85 to 230 K, and the desorption of fragments from the plasma-irradiated reddish colored ice was monitored. The TPD analysis was performed up to 230 K in this study, because the melting point of CH$_3$OH/H$_2$O (1:1 by volume) is approximately 230 K (Miller & Carpenter 1964). During the heating, the inner chamber was evacuated by the pumping system at 1 × 10^{-1} Pa while the mass spectrometer was operated around 3 × 10^{-5} Pa.

For the analysis for isotopic ice samples, 99% ^{13}CH$_3$OH (Wako pure chemical industries), 99.8% CD$_3$OD (Wako pure chemical industries), and 99.8% D$_2$O (Wako pure chemical industries) were utilized as purchased without further purification. The isotopic ice

samples were prepared by cooling ^{13}CH$_3$OH/H$_2$O, CD$_3$OD/H$_2$O, or CH$_3$OH/D$_2$O in 1:1 by volume from room temperature to 85 K, and then irradiated by the cryoplasma for 12 hr under the same conditions as the case of CH$_3$OH/H$_2$O ice sample. In all isotope-labeled experiments, the same appearance and disappearance of the reddish color were observed.

2.3. LC–MS and LC–MS/MS Analysis of the Residue

After the TPD analysis, the plasma-irradiated CH$_3$OH/H$_2$O ice was heated to room temperature, and the residue was collected for liquid chromatography mass spectroscopy (LC–MS) and the subsequent tandem mass spectroscopy (LC–MS/MS).
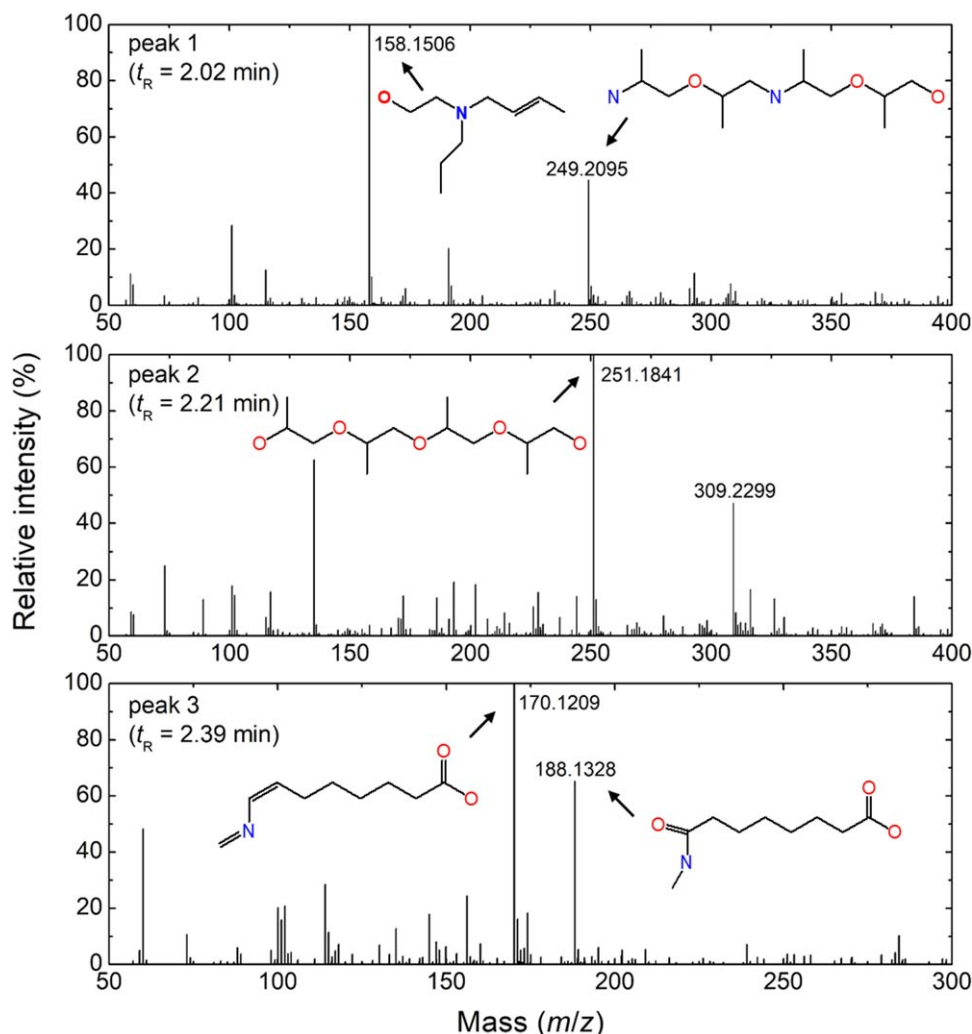
Figure 3. LC–MS spectra of the residue of the plasma-irradiated CH_3OH/H_2O ice at room temperature. Mass spectra corresponding to different retention times (t_R) of total ion chromatogram are shown in Appendix D, Figure 12. The chemical structures of representative peaks identified by MS/MS analysis (Appendix D, Figure 13) are also depicted.

Liquid chromatography was performed by an ultra-performance liquid chromatography system (Acquity UPLC, Waters Co., Ltd.) with a hydrophilic interaction chromatography (HILIC)-type column (Acquity UPLC BEH Amide, 2.1×150 mm, $1.7\,\mu$m, Waters Co., Ltd.). The column was kept at 40°C. The mobile phase was composed of two components: 0.1% formic acid and acetonitrile (5:95 by volume for the first 15 minutes and 50:50 by volume later). 10 μl of the residue was injected as picked up and flown at a speed of 0.2 ml minute^{-1}. Mass spectrometry was performed by a time-of-flight type mass spectrometer (Xevo QTof MS, Waters Co., Ltd.). Ionization of the sample was conducted by electrospray ionization at 3.0 kV capillary voltage and 30 V cone voltage. The mass spectrum range was 50–1000 m/z. The chemical formula of fragment ions from the mass spectra was estimated by their accurate masses. For peaks with strong intensity, subsequent tandem mass spectroscopy was conducted. Chemical structures in the mass spectra were estimated from both their accurate masses and the mass spectra of their peaks.

3. Results

During the irradiation of the cryoplasma, photographs of ice were taken from the upper side of the electrode for color

monitoring, and the optical emission from the cryoplasma was observed through the top electrode coated with transparent ITO (Figure 1(a)). We found that reddish coloration appeared on the ice and became more prominent with longer plasma irradiation (Figure 1(b)). On the other hand, the intensities of the optical emission lines from the cryoplasma decreased with time in the UV and visible range (Figure 1(c)). In other words, transmittance of the ice at UV and visible wavelengths decreased (Figure 1(c)), assuming constant emission intensity of the cryoplasma during the irradiation. This assumption is reasonable as the power consumption of cryoplasma during the irradiation was nearly constant (Appendix A, Figure 5). Therefore, the reddish color was attributed to the absorption by the product synthesized through the plasma irradiation. When using cryoplasma without N_2 gas flow as a control experiment, the reddish color was not observed visually (Appendix B, Figure 6). Thus, reactive nitrogen species from plasma, such as those identified in the emission spectrum of N_2^+ ions and excited N_2 molecules (shown in Figure 1(c)), should play a key role in the appearance of the reddish color.

To further analyze the reddish coloration, TPD experiments were performed. The post-plasma-irradiated ice was heated at 1 K minute^{-1} from 85 to 230 K at 1×10^{-1} Pa. The reddish color started fading at 120 K and subsequently disappeared at 150 K, as shown in Figure 2(a). The reddish color was not

reproduced when the temperature was conversely lowered from 165 to 85 K. It was still not reproduced when the same ice sample was subjected to 12 hr of the plasma irradiation at 175 K (Appendix B, Figure 7). In contrast, the reddish color was sustained when cooling the post-plasma-irradiated ice from 85 to 20 K (Appendix B, Figure 8). Therefore, the reddish color was specific to cryogenic temperatures. Since the disappearance of the reddish color was not reversible with respect to temperature, it might be due to the desorption of reddish substances and/or an irreversible chemical change of the reddish substance into colorless materials.

A quadrupole mass spectrometer was used to measure the desorption from the post-plasma-irradiated ice simultaneously with the reddish color disappearance. An increase in the intensity of the mass spectra signals was detected at some mass-to-charge ratio (m/z) in accordance with the disappearance of the reddish color. In particular, $m/z = 30$, 46, 60, 61, 72, and 73 showed noticeable increases, as shown in the TPD spectra in Figure 2(b). These m/z signals could correspond to fragments of desorbed reddish materials or byproducts derived from the transformation of reddish to colorless materials. To further investigate the desorption of substances that accompanied the color disappearance, TPD analysis for isotopic ice samples was also conducted. $^{13}CH_3OH/H_2O$ ice, CD_3OD/H_2O ice, and CH_3OH/D_2O ice were irradiated with the cryoplasma under the same conditions as described above. The m/z shifts between labeled and unlabeled methanol- and water-containing ice allowed estimation of the number of C or H atoms in the monitored substances.

Initially, signals at $m/z = 60$ and 61 showed clear shifts to higher m/z when methanol or water ices were isotopically labeled (right panel of Figure 2(c)). Carbon-13 labeling of methanol revealed that substances at $m/z = 60$ and 61 contained one methanol-derived C atom, while D labeling of methanol revealed two or four methanol-derived H atoms for $m/z = 60$ and three methanol-derived H atoms for $m/z = 61$. D labeling of water ice showed that both $m/z = 60$, 61 contained no water-derived H atom. Some possible molecular formulas of the substances that satisfy the isotopic analysis results are CH_2NO_2 or CH_4N_2O for $m/z = 60$ and CH_3NO_2 for $m/z = 61$. Both of these are nitrogen-containing unsaturated compounds that could possess $C = N$, $N = O$, or amide bonds, as shown in the possible chemical structures in Appendix C, Figure 9. Substances at $m/z = 72$ and 73 could possess unsaturated groups and/or nitrogen as well, as described in Appendix C.

This assignment of the fragments was consistent with the TPD and isotopic analysis for $m/z = 30$ and 46. The spectra at $m/z = 30$ and 46 did not show any shift in the peak positions when any of the isotopic labeled ice was used (left panel of Figure 2(c) and Appendix C, Figure 11). This implies that fragments at $m/z = 30$ and 46 do not contain any C or H atoms derived from methanol and water ice. Therefore, peaks at $m/z = 30$ and 46 likely stem from molecules composed entirely of N and O atoms, such as nitric oxide (NO) and nitrogen dioxide (NO_2), respectively. However, NO is colorless, and NO_2 converts to colorless dinitrogen tetroxide (N_2O_4) at lower temperatures below the melting point of N_2O_4 (261.9 K), although NO_2 appears to be reddish in color. Although NO_2 might be formed directly at cryogenic temperatures, the cryogenic presence of NO_2 is unclear because no data of NO_2 vapor pressure has been proposed (Fray & Schmitt 2009). Thus, tentatively, a plausible situation is these

nitrogen and oxygen containing compounds are fragments from our reddish materials.

The analysis of the colorless liquid residue obtained at room temperature supports the idea that nitrogen-containing and unsaturated organic compounds could have caused the reddish coloration. After heating the post-plasma-irradiated CH_3OH/H_2O ice to room temperature, the residue was analyzed by LC–MS and further mass spectroscopy (LC–MS/MS). Synthesis of various organic compounds with larger masses than the original CH_3OH/H_2O ice, such as glycols, carboxylic acids, amines, and amides, were identified as shown in Figures 3; see also Appendix D, Figure 13. Some of these compounds contain C=C and C=N bonds that absorb UV and visible radiation in the conjugated system, thus giving rise to a colored appearance. In terms of astrobiology, such structures and functional groups are essential building blocks of prebiotic organic molecules such as proteins (Bernstein et al. 2002; Munoz Caro et al. 2002) and genetic materials (Meinert et al. 2016). This implies that the observed reddish color is closely related to the possible existence of prebiotic organic compounds (Cruikshank et al. 2019), and especially prebiotic substances that can be stable only at cryogenic environments in the outer solar system.

4. Discussion

In the outer solar system, reddish colors have been explained by complex organic tholins, which contain delocalized electrons in the conjugated unsaturated bonds of aliphatic and aromatic hydrocarbons with some amounts of substituted nitrogen (Imanaka et al. 2004; Cruikshank et al. 2005). Excitation of delocalized electrons is accompanied by absorption at UV and visible wavelengths, which correspond to the reddish color. The reddish materials in this study can also be attributed to complex organic materials, considering the absorption at UV and visible wavelengths (Figure 1(c)) and the nitrogen-containing unsaturated fragments (Figures 2(b), (c)). However, the temperature-dependent behavior at cryogenic temperatures in this study has not been observed in previously reported reddish coloration of refractory tholins. This might imply a significant contribution of smaller and more volatile colorants to the appearance of cold surfaces in the outer solar system.

The color diversity of icy objects in the outer solar system, especially the absence of ultra-red coloration closer to the Sun, has been previously explained by the variation of compositions depending on the body environment (Jewitt 2002a; Grundy 2009; Sheppard 2010; Brown et al. 2011), with considering reddish organic tholins and colorless volatile species (Cruikshank et al. 2005). However, the explanation is not straightforward and still debatable because the well-known organic tholins are nonvolatile even when warming to room temperature. Here, the formation of the cryogenic-specific reddish coloration could offer a new possible explanation to the reddish color distribution in the outer solar system. The cryogenic-specific reddish materials disappear by sublimation or conversion to other colorless compounds at warmer cryogenic temperatures, as an icy body travels from the trans-Neptunian region to the inner solar system, such as Centaurs and thence the Jupiter-family region. This scenario implies that the body coloration and its diversity might be able to serve as a probe of current temperature and/or temperature history. The concept of reddish materials that are stable only at cryogenic temperatures is potentially useful for further investigation of color diversity observed in the outer solar system, including many reddish

objects, and would contribute to the further understanding of the nature and formation of the solar system.

To place our results in context with observational data of the color distribution of bodies in the outer solar system, we considered the color distribution of several Centaurs (Peixinho et al. 2003; Duffard et al. 2014) as a function of perihelion distance (see Appendix E). From this figure, we see that the ultra-red object closest to the Sun is in the 5–10 au range, with 31824 Elatus having the closest perihelion distance of 7.3 au (Duffard et al. 2014). No ultra-red objects have been found at distances less than 5–10 au (Jewitt 2002b). At such perihelion distances between the orbits of Jupiter and Saturn, the surface temperature of the bodies can reach to 120–150 K (Gilmore 2002; Bennett et al. 2013). This corresponds to the temperature range at which the reddish coloration faded and disappeared in our study. Therefore, our results and proposed scenario that reddish coloration of icy objects in the outer solar system could be explained by the presence of materials that are stable only at cryogenic temperatures are consistent with the observational data.

5. Conclusion

In this study, we demonstrated reddish coloration that is stable only at cryogenic temperatures by irradiating methanol- and water-containing ice with nitrogen-containing cryoplasma at 85 K. The reddish color visually faded and disappeared at 120–150 K as the ice was heated, unlike well-known refractory organic tholins that are stable even when heated to room temperature. By TPD analysis with isotopically labeled ices and LC–MS/MS analysis of the residue, the reddish material was suggested to be nitrogen-containing organic compounds. The temperature dependence of reddish coloration under cryogenic conditions could provide a new possible explanation for the absence of ultra-red coloration closer to the Sun in the outer solar system. Our result implies that a reddish material specific to cryogenic environments could be useful for the investigation of color diversity and formation mechanism of the outer solar system. Moreover, it is worthwhile to mention that cryoplasma was demonstrated to be a novel technology for accelerating the investigation of chemistry and materials science in cryogenic space environments including the outer solar system.

Appendix A
Characterization of the Cryoplasma

The current-voltage (I-V) characteristics of the cryoplasma was monitored during the plasma irradiation of CH_3OH/H_2O ice, as shown in Figure 4. Power consumption of the cryoplasma was calculated from the I-V characteristics as shown in Figure 5. The power consumption was stable within ± 0.4 mW. Therefore, the emission intensity of the cryoplasma during the 12 hr of irradiation was considered to be constant.
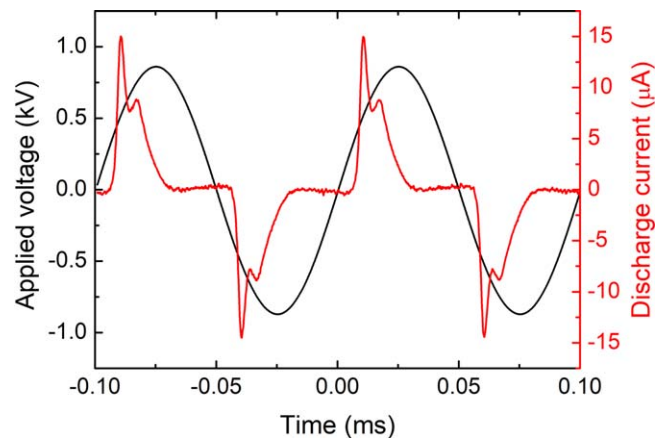

Figure 4. I–V characteristics of the cryoplsama. The black and red curves indicate the applied voltage to the electrode and the discharge current of the cryoplasma, respectively.
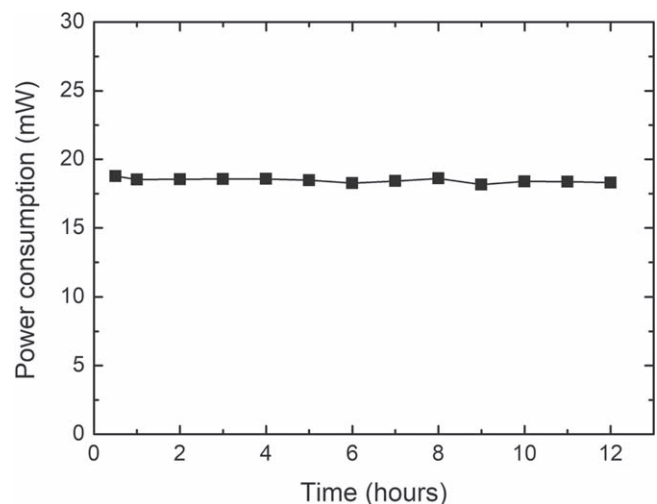

Figure 5. Temporal change in power consumption of the cryoplasma.

Appendix B
Control Experiment of the Cryoplasma Irradiation of CH$_3$OH/H$_2$O Ice

In order to evaluate the reddish coloration by the cryoplasma irradiation of CH$_3$OH/H$_2$O ice in Figures 1 and 2, two control experiments were performed, one without nitrogen gas flow (Figure 6), and another at 170 K (Figure 7). Cooling of the post-plasma-irradiated CH$_3$OH/H$_2$O ice from 85 to 20 K was also performed (Figure 8).
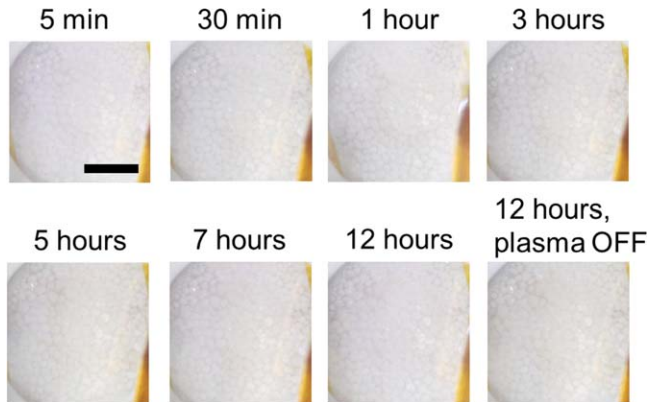

Figure 6. Photographs of the ice during the cryoplasma irradiation without nitrogen gas flow at 85 K. Photograph of the post-irradiation ice with the plasma turned off after 12 hr of irradiation is also illustrated. The scale bar is 5 mm. The plasma-irradiated ice did not show any visible color change when nitrogen gas was not introduced.
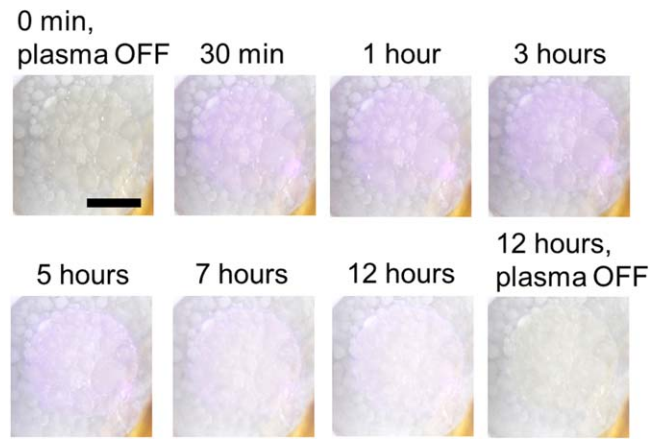

Figure 7. Photographs of the ice during the cryoplasma irradiation at 170 K. Photographs of the pre-irradiation and post-irradiation are also shown. The scale bar is 5 mm. The plasma-irradiated ice did not show any visible color change when irradiated at 170 K.
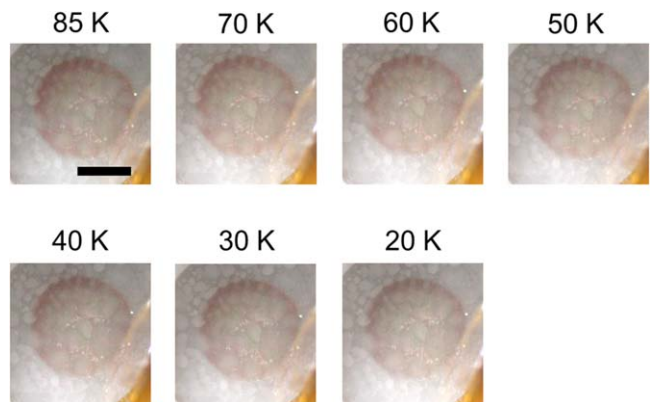

Figure 8. Cooling of the post-plasma-irradiated CH$_3$OH/H$_2$O ice. Photographs show that the reddish color was visibly maintained throughout the cooling to 20 K. The scale bar is 5 mm. The nonuniform reddish color was attributed to the nonuniform plasma generation at this time. The plasma was produced more strongly near the edge of the top electrode during this experiment.

Appendix C
Supporting Data of the TPD Analysis of the Plasma-irradiated Ice

To support the interpretation of the TPD analysis in the main text, examples of possible molecular formulae that satisfy the molecular masses for $m/z = 60$, 61, 72, and 73 (Figure 9), TPD spectra of the post-plasma-irradiated CH_3OH/H_2O ice for $m/z = 72–80$ (Figure 10), and mass spectra of the isotope-labeled analysis at different m/z ranges (Figure 11) are shown.
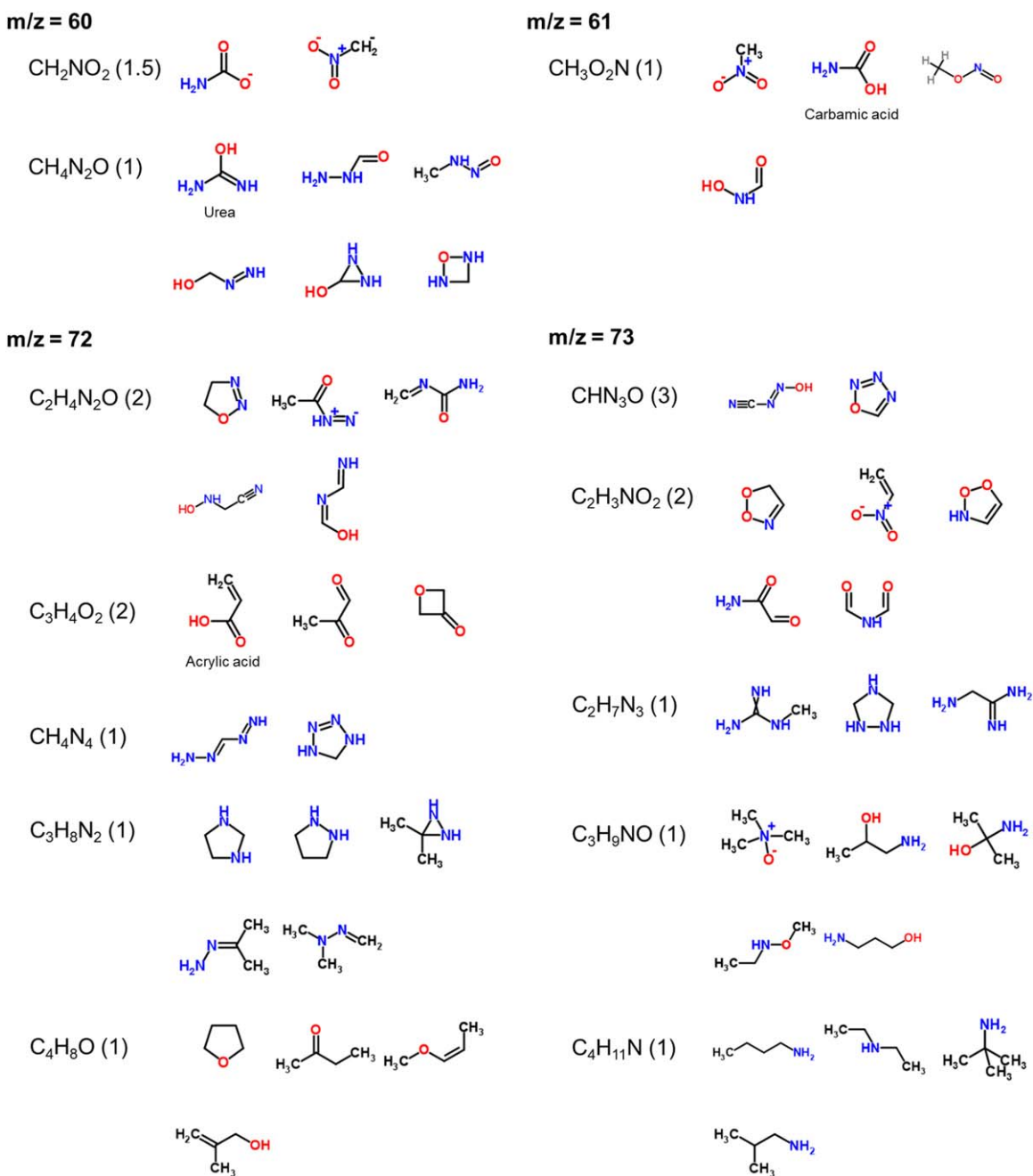

Figure 9. Examples of various molecular formulae satisfying the molecular masses. For $m/z = 60$ and 61, the molecular formula suggested above are also in good agreement with the results of isotopic analyses. The chemical structures are cited from a free chemical structure database ChemSpider (www.chemspider.com/). Numbers inside the parentheses indicate the degree of unsaturation.
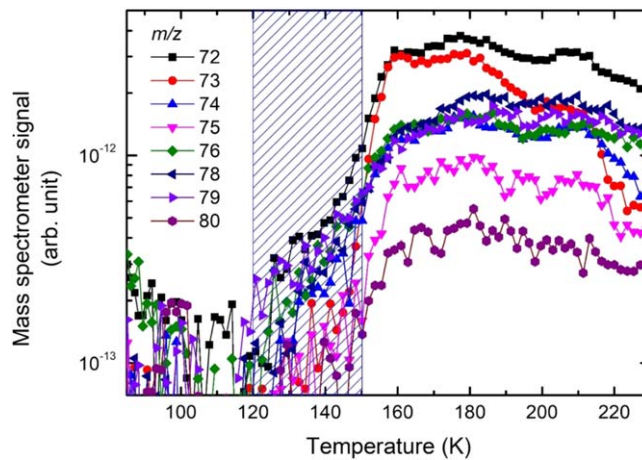
Figure 10. TPD spectra of the post-plasma-irradiated CH_3OH/H_2O ice for $m/z = 72$–80. The spectra for $m/z = 77$ could not be monitored correctly because of an inevitable noise from the QMS equipment.
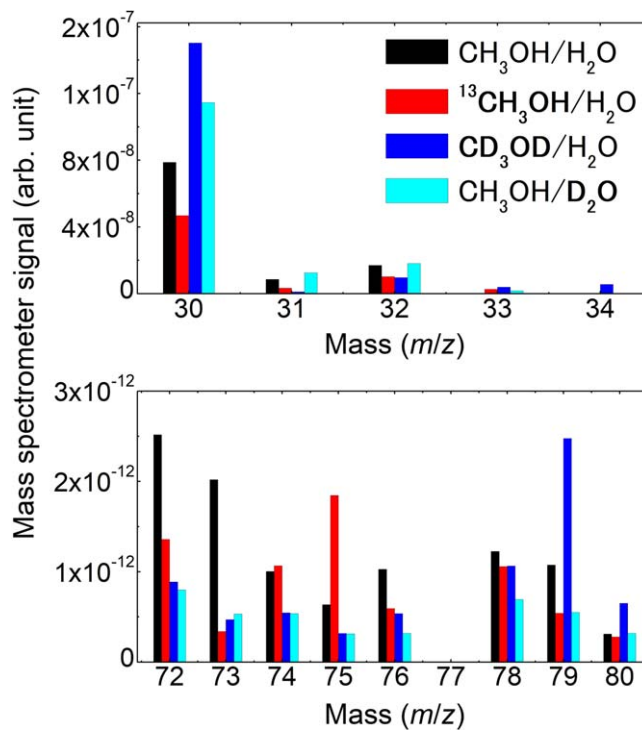

Figure 11. Mass spectra of the isotope-labeled analysis of the post-plasma-irradiated ice at different m/z ranges extended from the spectra in Figure 2(c). Mass spectra at 180 K are shown here. Isotopic analyses at $m/z = 30$ (top panel) showed similar shift in the peak positions as $m/z = 46$ (Figure 2(c)). Isotopic analyses at $m/z = 72$ and 73 (bottom panel) did not show clear shifts in the mass spectra peaks because fragments at higher masses ($m/z = 74$–80) also desorbed during the disappearance of the color (Figure 10), and their mass spectra signals increased. Various molecular formulas are possible for $m/z = 72$ and 73 as shown in Figure 9, some of which are unsaturated and/or nitrogen containing.

Appendix D
Supporting Data of the LC-MS and LC-MS/MS Analysis of the Residue

To support the LC-MS and LC-MS/MS analysis of the residue in the main text, total ion chromatogram by liquid chromatography of the sample residue at room temperature (Figure 12), and LC-MS/MS spectra of the peaks at $m/z = 158$, 170, 188, 249, and 251 in the LC-MS spectra in Figure 3 (Figure 13) are shown.
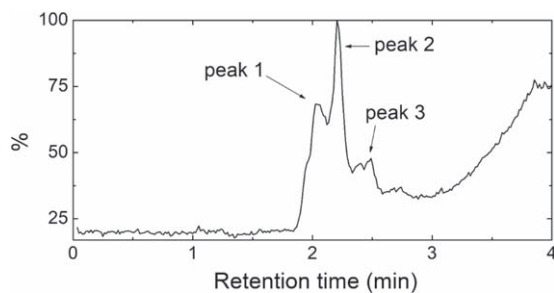
Figure 12. Total ion chromatogram by the liquid chromatography of the sample residue at room temperature. Further mass spectroscopy was performed for the peaks of different retention times (t_R), i.e., peak 1 at $t_R = 2.02$ minutes, peak 2 at $t_R = 2.21$ minutes, and peak 3 at $t_R = 2.39$ minutes.
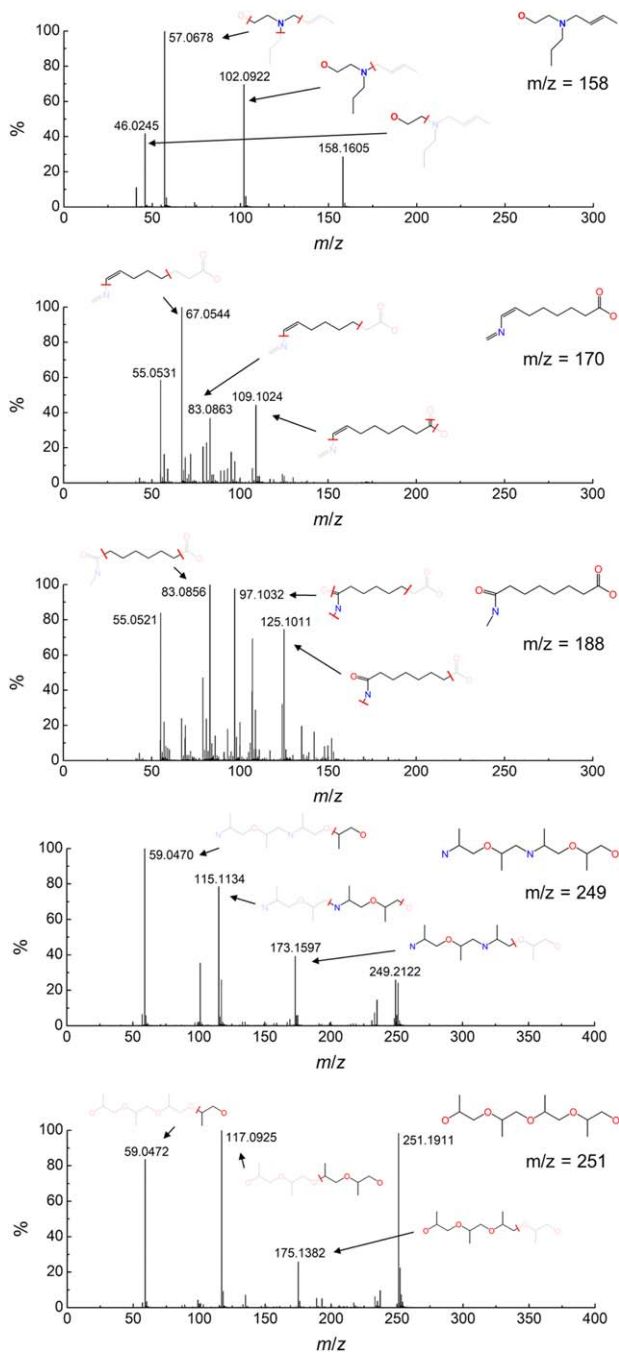

Figure 13. LC–MS/MS spectra of the peaks at $m/z = 158$, 170, 188, 249, and 251 in the LC–MS spectra in Figure 3. MS/MS analysis was carried out to estimate chemical structures of the peaks by monitoring the fragments from the substance of the target m/z peak. The chemical structures of fragments estimated for the observed MS–MS spectra peaks are also depicted.
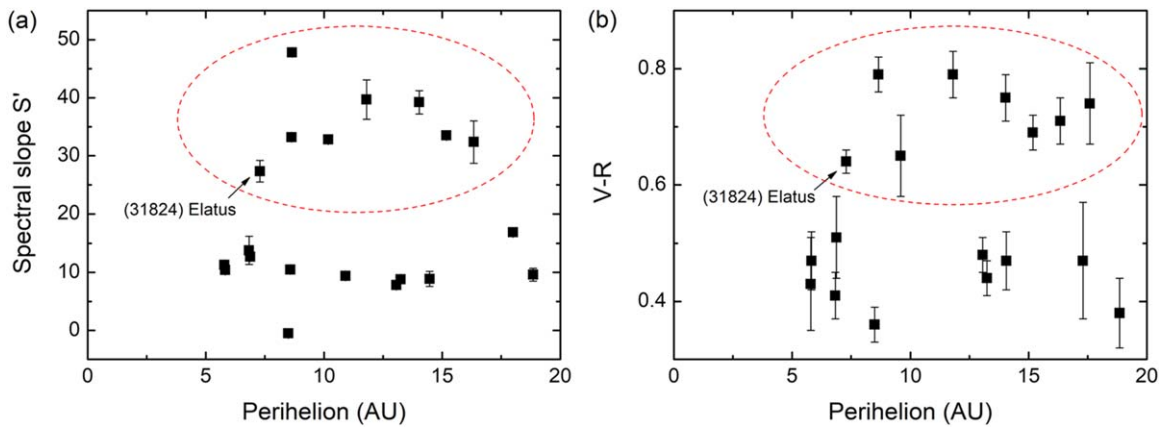
Figure 14. Color distribution of Centaurs at different perihelion distances. (a) Spectral slope (S') vs. perihelion distances. The presented data were taken from Duffard et al. (2014). (b) $V - R$ color index vs. perihelion distances. The presented data were taken from Peixinho et al. (2003). The red dashed circles indicate ultra-red objects with $S' > 27$ or $V - R > 0.6$, respectively.

Appendix E
Observational Data of the Color Distribution in the Outer Solar System

To compare our results with observations, plots of the color distribution of Centaurs at different perihelion distances were made based on the observational data in Duffard et al. (2014) and Peixinho et al. (2003), as shown in Figure 14. In both plots, 31824 Elatus, with a perihelion distance of 7.3 au, is the closest body that shows an ultra-red color.

ORCID iDs

Noritaka Sakakibara ⦿ https://orcid.org/0000-0002-3910-6553
Tsuyohito Ito ⦿ https://orcid.org/0000-0001-9935-7701
Kazuo Terashima ⦿ https://orcid.org/0000-0003-2283-2396

References

Bagenal, F., Horanyi, M., McComas, D. J., et al. 2016, Sci, 351, aad9045
Bennett, C. J., Pirim, C., & Orlando, T. M. 2013, ChRv, 113, 9086
Bernstein, M. P., Dworkin, J. P., Sandford, S. A., Cooper, G. W., & Allamandola, L. J. 2002, Natur, 416, 401
Brown, M. E., Schaller, E. L., & Fraser, W. C. 2011, ApJL, 739, L60
Brunetto, R., Barucci, M. A., Dotto, E., & Strazzulla, G. 2006, ApJ, 644, 646
Cruikshank, D. P., Imanaka, H., & Dalle Ore, C. M. 2005, AdSpR, 36, 178
Cruikshank, D. P., Materese, C. K., Pendleton, Y. J., et al. 2019, AsBio, 19, 831
Dalle Ore, C. M., Barucci, M. A., Emery, J. P., et al. 2015, Icar, 252, 311

Dalle Ore, C. M., Fulchignoni, M., Cruikshank, D. P., et al. 2011, A&A, 533, A98
Duffard, R., Pinilla-Alonso, N., Santos-Sanz, P., et al. 2014, A&A, 564, A92
Duncan, M. J., & Levison, H. F. 1997, Sci, 276, 1670
Fray, N., & Schmitt, B. 2009, P&SS, 57, 2053
Gilmore, D. G. 2002, Spacecraft Thermal Control Handbook, Volume I: Fundamental Technologies (2nd ed.; California: The Aerospace Press), 50
Grundy, W. M. 2009, Icar, 199, 560
Imanaka, H., Khare, B. N., Elsila, J. E., et al. 2004, Icar, 168, 344
Jewitt, D. 2002a, AJ, 150, 201
Jewitt, D. C. 2002b, AJ, 123, 1039
Khare, B. N., Sagan, C., Ogino, H., et al. 1986, Icar, 68, 176
Lewis, J. S. 1973, SSRv, 14, 401
Lowry, S., Fitzsimmons, A., Lamy, P., & Weissman, P. 2008, in The Solar System Beyond Neptune, ed. A. Barucci et al. (Tucson, AZ: Univ. Arizona Press), 397
Luu, J., & Jewitt, D. 1996, AJ, 112, 2310
Materese, C. K., Cruikshank, D. P., Sandford, S. A., et al. 2014, ApJ, 788, 111
Materese, C. K., Cruikshank, D. P., Sandford, S. A., Imanaka, H., & Nuevo, M. 2015, ApJ, 812, 150
Meinert, C., Myrgorodska, I., Marcellus, P., et al. 2016, Sci, 352, 208
Miller, G. A., & Carpenter, D. K. 1964, J. Chem. Eng. Data, 9, 371
Munoz Caro, G. M., Meierhenrich, U. J., Schutte, W. A., et al. 2002, Natur, 416, 403
Peixinho, N., Doressoundiram, A., Delsanti, A., et al. 2003, A&A, 410, L29
Sakakibara, N., Ito, T., & Terashima, K. 2019, Langm, 35, 3013
Sakakibara, N., & Terashima, K. 2017, JPhD, 50, 22LT01
Sheppard, S. S. 2010, AJ, 139, 1394
Stauss, S., Muneoka, H., & Terashima, K. 2018, PSST, 27, 023003
Stern, S. A., Bagenal, F., Enicco, K., et al. 2015, Sci, 350, aad1815
Stern, S. A., Weaver, H. A., Spencer, J. R., et al. 2019, Sci, 364, eaaw9771
Thompson, W. R., Henry, T. J., Schwartz, J. M., Khare, B. N., & Sagan, C. 1991, Icar, 90, 57
Weaver, H. A., Buie, M. W., Buratti, B. J., et al. 2016, Sci, 351, aae0030